

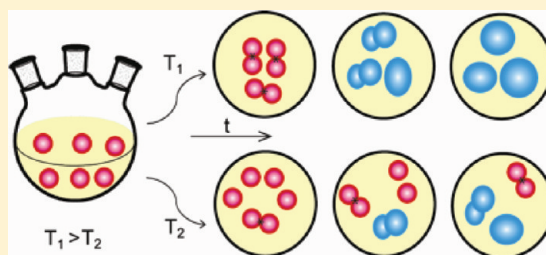
# Phase Transformation of Colloidal $\text{In}_2\text{O}_3$ Nanocrystals Driven by the Interface Nucleation Mechanism: A Kinetic Study

Shokouh S. Farvid and Pavle V. Radovanovic\*

Department of Chemistry and Waterloo Institute for Nanotechnology, University of Waterloo, 200 University Avenue West, Waterloo, Ontario N2L 3G1, Canada

## Supporting Information

**ABSTRACT:** The kinetics of phase transformation of colloidal  $\text{In}_2\text{O}_3$  nanocrystals (NCs) during their synthesis in solution was explored by a combination of structural and spectroscopic methods, including X-ray diffraction, transmission electron microscopy, and extended X-ray absorption fine structure spectroscopy. Johnson–Mehl–Avrami–Erofev–Kholmogorov (JMAEK) and the interface nucleation models were used to analyze the isothermal kinetic data for the phase transformation of NCs in the temperature range of 210–260 °C. The results show that NCs are initially stabilized in the metastable corundum (rh- $\text{In}_2\text{O}_3$ ) phase. The phase transformation occurs via nucleation of cubic bixbyite (bcc- $\text{In}_2\text{O}_3$ ) phase at the interface between contacting rh- $\text{In}_2\text{O}_3$  NCs, and propagates rapidly throughout the NC volume. The activation energy of the phase transformation was determined from the Arrhenius expression to be  $152 \pm 60$  kJ/mol. The interface nucleation rate is maximal at the beginning of the phase transformation process, and decreases over the course of the reaction due to a decrease in the concentration of rh- $\text{In}_2\text{O}_3$  NCs in the reaction mixture. In situ high-temperature XRD patterns collected during nonisothermal treatment of  $\text{In}_2\text{O}_3$  NCs reveal that phase transformation of smaller NCs occurs at a faster rate and lower temperature, which is associated with their higher packing density and contact formation probability. Because NC surfaces and interfaces play a key role in phase transformation, their control through the synthesis conditions and reaction kinetics is an effective route to manipulate NC structure and properties.



## INTRODUCTION

Detailed understanding of the correlation between the growth and phase transformation mechanisms of nanocrystals (NCs) creates an opportunity to discover the pathways that lead to metastable high-energy structures,<sup>1–3</sup> thereby expanding the means to manipulate functional properties of solid-state materials. The thermodynamics and kinetics of phase transformations of NCs have largely been studied under extreme conditions (high pressure and temperature).<sup>2,4</sup> These studies have provided quantitative information about the phase transformation, including the activation barriers between different crystal structures.<sup>2</sup> It is now well-known that the thermodynamic phase stability of solids can be spontaneously reversed below critical sizes.<sup>5,6</sup> The reversal of the phase stability in nanocrystalline materials has been associated with large surface to volume ratios in reduced dimensions. The high surface area of nanostructures can lead to the spontaneous stabilization of metastable phases owing to the surface energy and/or surface stress contributions, both of which are dependent on size.<sup>5</sup>

Transparent conducting oxides (TCOs) have been commercially exploited for the fabrication transparent electrodes in optoelectronic devices, such as photovoltaic cells, flat panel displays, and sensors, due to their transparency to visible light, electrical conductivity and inertness.<sup>7,8</sup> Most TCOs are polymorphic, which makes them good model systems for the

fundamental studies of phase transformation in solid state, and allows for the control of their functional properties by structural manipulation. Indium oxide is a wide band gap ( $E_g \approx 3.7$  eV) semiconductor, characterized by high charge carrier concentration and mobility,<sup>9</sup> as well as the ease with which it can be deposited as a thin film.<sup>10</sup> The polymorphs of  $\text{In}_2\text{O}_3$  are crystallized in the cubic bixbyite-type crystal structure (bcc- $\text{In}_2\text{O}_3$ , bcc = body-centered cubic) under ambient conditions, and the corundum-type structure (rh- $\text{In}_2\text{O}_3$ , rh = rhombohedral) under high pressure and temperature.<sup>11–13</sup> The stabilization of rh- $\text{In}_2\text{O}_3$  under atmospheric pressure has been achieved by annealing of crystalline  $\text{In}(\text{OH})_3$ ,<sup>14,15</sup> or  $\text{InOOH}$  nanofibers<sup>16</sup> and nanotubes.<sup>17</sup> The synthesis of colloidal rh- $\text{In}_2\text{O}_3$  NCs has been reported by rapid dehydration of small  $\text{InOOH}$  nanoparticles prepared by a surfactant-assisted method,<sup>18</sup> or by simple control of the NC size below ca. 5 nm via the growth kinetics.<sup>19</sup> Although the synthesis of metastable rh- $\text{In}_2\text{O}_3$  has been an increasingly active area of research in recent years, to our knowledge, there has been no quantitative kinetic or mechanistic study of the phase transformation of colloidal  $\text{In}_2\text{O}_3$  NCs in solution.

Different nucleation and nuclei growth models have been used to describe the kinetics of solid-state reactions.<sup>20–22</sup> The

Received: December 13, 2011

Published: March 26, 2012

nucleation and nuclei growth models for solid-state reactions and phase transformations assume that nucleation sites are randomly distributed within the lattice of the original phase.<sup>21,22</sup> This assumption does not exclude the possibility of preferential nuclei formation at particular sites in the original phase, and only requires that these active sites be randomly distributed. One of the models widely used to describe solid-state phase transformations is the Johnson–Mehl–Avrami–Erofev–Kholmogorov (JMAEK) model,<sup>20,23–25</sup> which correlates the phase transformation kinetics to the nucleation and growth rates of the newly formed phase, taking into account the coalescence and ingestion of the nuclei.<sup>20</sup> Although the JMAEK model is applicable to many solid-state reactions, it assumes that samples have infinite size,<sup>26,27</sup> which makes this model physically unrealistic for nanocrystalline materials.<sup>28</sup> Other models have therefore been developed to describe phase transformations of NCs based on the known or assumed mechanistic details. Notable examples include surface and interface nucleation models. The common assumption in these models is that defect sites either at the surfaces of NCs or at the interfaces between contacting NCs serve as nucleation sites for the formation of a new phase.<sup>20,29</sup> However, it has been found that the correct value of the activation energy ( $E_a$ ) for the isothermal kinetic data can be extracted using any model.<sup>30,31</sup> Employing conventional models such as JMAEK therefore remains a good approach for obtaining the kinetic parameters from the isothermal measurements in cases for which a precise model is not available. The kinetic studies of phase transformation of  $\text{TiO}_2$  NCs have suggested a strong size dependence of the phase transformation.<sup>32,33</sup> Bulk  $\text{TiO}_2$  is thermodynamically stable in the rutile phase, whereas anatase becomes more stable than rutile for NC sizes below ca. 14 nm.<sup>5,34</sup> Zhang et al.<sup>28,29,33</sup> proposed interface and surface nucleation models for the phase transformation of  $\text{TiO}_2$  NCs under different conditions. The interface nucleation mechanism, for which a new phase is formed at the NC–NC contacts, occurs at low reaction temperatures and high packing density of NCs. For low packing density of NCs, a new phase forms at the surfaces of the old phase (surface nucleation mechanism). Once the new phase is nucleated, the transformation can quickly spread through NCs.<sup>28,29</sup>

In this article, we report a detailed kinetic study of the phase transformation of colloidal rh- $\text{In}_2\text{O}_3$  to bcc- $\text{In}_2\text{O}_3$  NCs during their growth in solution. The correlation between the rates of NC growth and phase transformation was established, indicating size-dependent metastable phase stabilization and transformation. The structural information about the reaction products at different times during the synthesis were obtained from the X-ray diffraction (XRD) and X-ray absorption spectroscopy (XAS) measurements and analyzed using JMAEK and interface nucleation models. The extracted activation energies were nearly identical ( $E_a \approx 152$  kJ/mol), confirming independence of  $E_a$  on the kinetic model for the isothermal kinetic data. The kinetic analysis in conjunction with the electron microscopy results suggests the dominant interface nucleation mechanism. The effect of the NC interactions on the phase transformation of  $\text{In}_2\text{O}_3$  NCs and the role of surface stress in this process are also discussed. The mechanistic results of this work allow for a rational optimization of the reaction conditions for the synthesis of colloidal  $\text{In}_2\text{O}_3$  NCs as building blocks with a desired crystal structure, and contribute to the general understanding of the structural transformation and property control in the solid state.

## ■ EXPERIMENTAL SECTION

**Chemicals and Solvents.** All reagents were used as received. Indium acetylacetonate ( $\text{In}(\text{acac})_3$ ; 98%) and indium nitrate hydrate ( $\text{In}(\text{NO}_3)_3 \cdot x\text{H}_2\text{O}$ ; 99.999%) were purchased from Strem Chemicals. Oleylamine (70%) and tri-*n*-octylphosphine oxide (TOPO; 90%) were purchased from Sigma-Aldrich Company, toluene (99.98%) was purchased from EMD Chemicals, and hexane (99.9%) from Fischer Scientific.

**Synthesis of  $\text{In}_2\text{O}_3$  NCs.** The kinetic study of the phase transformation of  $\text{In}_2\text{O}_3$  NCs was performed using the synthesis method described elsewhere.<sup>19</sup> In a typical reaction, 4 mmol of  $\text{In}(\text{acac})_3$  and 48 mmol of oleylamine were mixed in a 100 mL three-neck round-bottom flask and magnetically stirred for 15 min under a flow of argon. The reaction mixture was then heated to a desired temperature in the argon atmosphere. The heating rate was controlled so that the reaction mixture reaches the desired temperature after 1 h. The reaction mixture was then refluxed at the final temperature and the portions of the obtained product were taken at different times during the reaction. For nonisothermal kinetic investigations in solution, the reaction mixture was allowed to reach 240 °C while stirring for 1 h, and with the heating continuing at the rate of 1 °C/min, the aliquots were taken in the temperature range 250–280 °C. The obtained samples were gradually cooled to room temperature under argon at the rate of 3 °C/min, and the NCs were precipitated and washed three times with ethanol.

For in situ nonisothermal XRD study of the phase transformation of larger (ca. 5 nm) rh- $\text{In}_2\text{O}_3$  NCs, the sample was prepared in the powder form by the alcoholysis method, according to the previously reported procedure.<sup>35</sup> In this synthesis, 1 mmol of  $\text{In}(\text{NO}_3)_3$  in 50 mL of ethanol was stirred for 30 min. The same volume of 0.15 M NaOH solution in ethanol was added to the reaction mixture and the obtained  $\text{In}(\text{OH})_3$  precipitate was washed with ethanol, dried in air, and finally calcined to obtain rh- $\text{In}_2\text{O}_3$  NCs.

**Measurements and Data Analysis.** Transmission electron microscopy (TEM) imaging was performed with a JEOL-2010F microscope operating at 200 kV. The specimens were prepared by dropping dilute suspensions of colloidal NCs in toluene on copper grids with lacey Formvar/carbon support films purchased from Ted Pella, Inc. The absorption spectra were collected with a Varian Cary 5000 UV–vis–NIR spectrophotometer. Photoluminescence (PL) spectra were recorded with a Varian Cary Eclipse fluorescence spectrometer. For photoluminescence measurements, the precipitated NCs were heated in molten TOPO at 90 °C, reprecipitated, and washed with ethanol. The TOPO-capped NCs were dispersed in hexane.

Powder X-ray diffraction (XRD) patterns were collected with an INEL powder diffractometer equipped with a position-sensitive detector, using monochromatic  $\text{Cu K}\alpha$  radiation. The in situ nonisothermal phase transformation was investigated by XRD measurements in the argon atmosphere, using the same diffractometer fitted with a high-temperature reaction chamber. The samples were preheated in the chamber to 240 °C with a heating rate of 5 °C/min. Upon temperature stabilization, the sample was heated at the same rate to different temperatures, and upon reaching the desired temperature, the XRD pattern was recorded for 15 min. We performed the linear combination and deconvolution analyses to determine the phase contents of  $\text{In}_2\text{O}_3$  NC samples synthesized between 0 and 30 h in the temperature range 210–260 °C. For the linear combination analysis, we used rh- $\text{In}_2\text{O}_3$  and bcc- $\text{In}_2\text{O}_3$  NCs obtained with high purity in the 30 h reaction at 200 °C and 7 h reaction at 230 °C, respectively, as references. The phase contents of the samples synthesized in the temperature range 210–260 °C for different durations were determined by matching their XRD patterns to the linear combination of the reference XRD patterns. For the deconvolution method, the phase contents of  $\text{In}_2\text{O}_3$  NCs were calculated by fitting the overlapped bcc- $\text{In}_2\text{O}_3$  (222) and (400), and rh- $\text{In}_2\text{O}_3$  (104) and (110) peaks. The intensities of the four peaks were set proportionally to their standard intensities based on the JCPDS

cards of these two phases. The weight fraction of bcc-In<sub>2</sub>O<sub>3</sub> ( $W_{\text{bcc}}$ ) can be calculated from:

$$W_{\text{bcc}} = \frac{A_{\text{bcc}}}{A_{\text{bcc}} + 3.4A_{\text{rh}}} \quad (1)$$

where  $A_{\text{bcc}}$  and  $A_{\text{rh}}$  are the integrated intensities of the bcc-In<sub>2</sub>O<sub>3</sub> (222) and rh-In<sub>2</sub>O<sub>3</sub> (104) peaks, respectively. The integrated intensity ratio for the bcc-In<sub>2</sub>O<sub>3</sub> (222) peak to the rh-In<sub>2</sub>O<sub>3</sub> (104) peak obtained from the XRD pattern of the two references is 3.4.

The X-ray absorption spectroscopy (XAS) measurements were performed at 06ID-1 beamline at the Canadian Light Source (CLS). The Si (220) crystal was used as an X-ray beam monochromator, and the harmonics rejection was achieved by detuning the second monochromator crystal by 60%. Indium K-edge energy calibration was carried out using the Sn foil standard (K-edge at 29200 eV). For In<sub>2</sub>O<sub>3</sub> NC samples, the spectra were recorded in the transmission mode with three ionization chambers. The first and second ionization chambers were used to monitor the incident and transmitted X-ray intensities, respectively. The third ionization chamber was used in conjunction with the Sn foil standard to provide internal calibration for the In K-edge position. Extended X-ray absorption fine structure (EXAFS) data analysis was performed using the Cherokee and RoundMidnight codes from the "Multiplatform Applications for the XAFS" (MAX) package.<sup>36</sup> EXAFS data were analyzed according to the previously described procedure.<sup>37</sup> Structural parameters, including the coordination number ( $N$ ), bond length ( $R$ ), and the Debye–Waller factor ( $\sigma^2$ ) were obtained from the EXAFS spectra analysis.

## RESULTS AND DISCUSSION

Figure 1 shows XRD patterns and the corresponding NC size distribution histograms derived from the TEM images of the samples synthesized at 230 (a) and 260 °C (b) for different reaction times. The full assignment of the XRD reflections is shown in Figure S1 (Supporting Information). Broadening of the XRD peaks is evident for short reaction times at both temperatures. For longer reaction times XRD peak broadening decreases, indicating an increase in the average NC size. From the TEM images of NCs synthesized at 230 °C (Figure S2, Supporting Information), the average NC sizes immediately upon reaching the final temperature (0 min) and after 7 h of heating were determined to be ca. 2.5 and 7.3 nm, respectively. The increase in NC size occurs concurrently with a change in the crystal structure from rh-In<sub>2</sub>O<sub>3</sub> to bcc-In<sub>2</sub>O<sub>3</sub>. For the reaction times up to 10 min, only NCs smaller than 5 nm were observed, which are largely stabilized as rh-In<sub>2</sub>O<sub>3</sub>. On the other hand, the NC product isolated after 7 h has predominantly bcc-In<sub>2</sub>O<sub>3</sub> structure. We have previously reported the spontaneous stabilization of rh-In<sub>2</sub>O<sub>3</sub> phase for NCs below the critical size of ca. 5 nm, which has been associated with surface energy and/or surface stress contribution.<sup>19,38,39</sup> Given the structural and thermodynamic similarity of the two phases,<sup>13</sup> surface stress could be a particularly important effect causing an excess pressure and favoring the stabilization of rh-In<sub>2</sub>O<sub>3</sub> NCs due to a slightly higher density of corundum relative to cubic bixbyite phase. The XRD peaks of the sample synthesized at 260 °C (Figure 1b) indicate a mixture of the two crystal structures at the beginning of the reaction. In addition, the size distribution histogram at 0 min shows a bimodal NC size distribution, with small NCs having an average size of ca. 3.3 nm, and large NCs of ca. 5.6 nm. Increase in the reaction time results in an increase in the ratio of large-to-small NCs, and a more dominant presence of the bcc-In<sub>2</sub>O<sub>3</sub> phase. After 1 h bcc-In<sub>2</sub>O<sub>3</sub> NCs having an average size of ca. 8.2 nm were isolated. At both temperatures an increase in the reaction time causes an increase in the fraction of large NCs at the expense of the small ones.

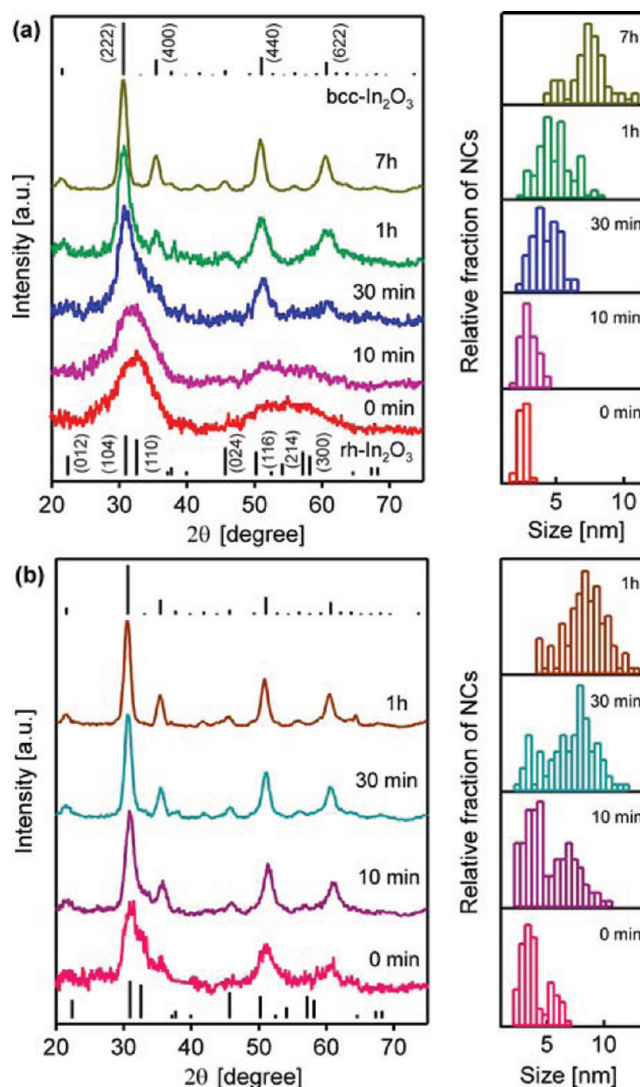


**Figure 1.** XRD patterns (left) and the corresponding size distribution histograms (right) of the samples synthesized at (a) 230 °C and (b) 260 °C for different reaction times (indicated in the graphs). The vertical lines in the XRD patterns are XRD peak positions of bulk rh-In<sub>2</sub>O<sub>3</sub> (bottom, JCPDS 21-0406) and bcc-In<sub>2</sub>O<sub>3</sub> (top, JCPDS 06-0416). The size distribution histograms were derived from the TEM images collected at the same magnification, by measuring the sizes of 200 NCs for each sample.

Faster NC growth at higher temperature is accompanied by an increase in the rate of phase transformation from rh-In<sub>2</sub>O<sub>3</sub> to bcc-In<sub>2</sub>O<sub>3</sub> phase.

The quantitative analysis of the kinetics of phase transformation was performed using the most pronounced XRD peaks in the region  $2\theta \approx 25\text{--}40^\circ$ . In this range, the XRD patterns consist of a mixture of bcc-In<sub>2</sub>O<sub>3</sub> (222) and (400), and rh-In<sub>2</sub>O<sub>3</sub> (104) and (110) reflections. The deconvolution of the XRD peaks of the sample synthesized at 250 °C for 20 min is shown in Figure 2a, as an example. In the deconvolution analysis, fitting to the experimental data was performed using the initial values for the peak broadenings defined based on the average NC sizes obtained from TEM images (Table S1, Supporting Information). The best fit to the experimental data in Figure 2a corresponds to 86% rh-In<sub>2</sub>O<sub>3</sub> and 14% bcc-In<sub>2</sub>O<sub>3</sub> phase. The phase content determination was also performed by linear combination analysis using XRD patterns of pure phase



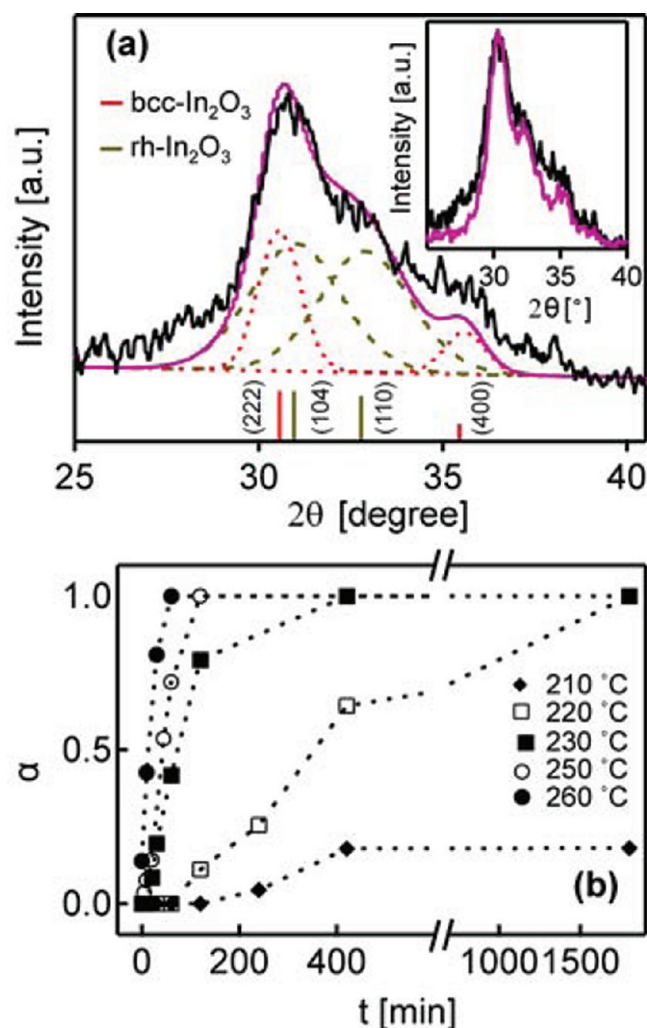


**Figure 2.** (a) Narrow-range XRD pattern of the sample synthesized at 250 °C for 20 min (solid black trace), and the deconvoluted (222) and (400) peaks of bcc-In<sub>2</sub>O<sub>3</sub> (dotted red trace), and (104) and (110) peaks of rh-In<sub>2</sub>O<sub>3</sub> (dashed olive trace). The pink trace is the superposition of the deconvoluted peaks. Inset: linear combination fitting (solid pink line) of the reference samples for the same XRD range. (b) Average content of bcc-In<sub>2</sub>O<sub>3</sub> followed over 30 h for the reactions at different temperatures from 210 to 260 °C.

NC samples. The linear combinations of the XRD patterns of the reference samples were well-matched to the experimental patterns obtained for the analogous mixtures of these references, justifying this complementary approach to the analysis of XRD data (Figure S3, Supporting Information). The inset in Figure 2a shows the best linear combination fit for the same XRD data. The results of the peak deconvolution and linear combination were in a very good agreement for all samples, and the phase content for the kinetic analysis was derived as an average content from the two approaches. These phase content results were also confirmed by the EXAFS linear combination fitting (Figure S4, Supporting Information). Figure 2b shows the content of bcc-In<sub>2</sub>O<sub>3</sub> ( $\alpha$ ) over 30 h for reactions in the temperature range 210–260 °C. The evolution of the average sizes of rh-In<sub>2</sub>O<sub>3</sub> and bcc-In<sub>2</sub>O<sub>3</sub> NCs in the same samples, determined from the full width at half-maximum (fwhm) of the peaks obtained by the deconvolution method, are shown in Figure S5 (Supporting Information). The NC sizes determined from the final peak broadening, as a fitting

parameter in the deconvolution analysis, remain in good agreement with the average NC sizes obtained from TEM images (Table S1). A qualitative comparison of the kinetic behavior of NC growth (Figure S5) and phase transformation (Figure 2b) reveals the same trend, indicating a correlation between these two processes.

The phase transformation kinetics was studied by a generic JMAEK model, which is frequently used to describe solid-state phase transformations.<sup>20,23</sup> In this model, the reaction progress ( $\alpha$ ) has a sigmoidal dependence on time,<sup>20</sup> as the reaction at first has a slow rate, followed by a faster one, and then slow again.<sup>23</sup> As a consequence, there is a bell-shaped relationship between the reaction rate ( $d\alpha/dt$ ) and  $\alpha$ . The JMAEK equation can be written as:

$$-\ln(1 - \alpha) = (kt)^n \quad (2)$$

where  $k$  is the rate constant of the reaction at time ( $t$ ) and  $n$  is an exponent.<sup>20</sup> Figure S6 (Supporting Information) shows the rate of formation of the bcc-In<sub>2</sub>O<sub>3</sub> phase as a function of  $\alpha$  at various reaction temperatures. The bell-shaped functional forms are consistent with the sigmoidal  $\alpha$ - $t$  curves, and justify the use of JMAEK model.<sup>20</sup> Figure 3a plots the phase content data for

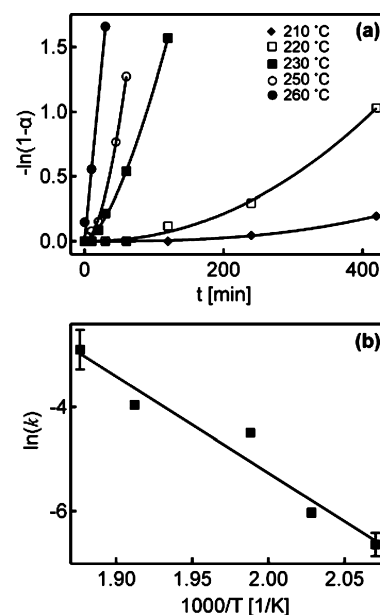


**Figure 3.** (a) JMAEK plots generated from the fraction of the bcc-In<sub>2</sub>O<sub>3</sub> phase ( $\alpha$ ) present at different points in time in the samples synthesized at different temperatures. (b) Arrhenius plot based on the rate constants obtained from the JMAEK plot.

In<sub>2</sub>O<sub>3</sub> NCs (the left-hand side of eq 2) as a function of time for five different temperatures. The data are well fit with JMAEK equation (solid lines), with the rate constant  $k$  and the exponent  $n$  as adjustable parameters. The plots of  $\ln[-\ln(1 - \alpha)]$  versus  $\ln(t)$  show linear behavior (Figure S6, Supporting Information), allowing for the extraction of the same parameters, and the confirmation of the obtained results. The values of the exponents and rate constants are summarized in Table 1. The exponent  $n$  decreases with increasing temperature from 2.6 to 1, in the studied temperature range (210–260 °C). According to the diffusion-controlled nuclei growth models,  $n$  is a function of the geometry of nuclei (dimensional factor,  $\lambda$ , which can be 1, 2, or 3) and the nucleation probability (nucleation factor,  $\beta$ , where  $0 < \beta < 1$ ),<sup>24</sup> and can be expressed

Table 1. Values of  $n$  and  $k$  Obtained from the JMAEK Plot

$T$ (°C)	$n$	$k$ (min <sup>-1</sup> )
210	2.6	0.0013
220	1.7	0.0024
230	1.6	0.0112
250	1.4	0.0190
260	1.0	0.0552

as  $n = \beta + \lambda/2$ . Noninteger values of  $n$  in the range of 1.5–2.5 have been attributed to the diffusion-controlled mechanism for three-dimensional (quasi-spherical particle) growth, with decreasing nucleation rate over the course of the reaction.<sup>21,22</sup> Lower  $n$  values ( $n < 1.5$ ) are characteristic for the zero nucleation rate mechanism, or a process in which all nucleation events occur very rapidly at the initial stage, followed by the nuclei growth. In the context of these considerations, the  $n$  values calculated in this study suggest that the nucleation of bcc-In<sub>2</sub>O<sub>3</sub> phase occurs uniformly on quasi-spherical rh-In<sub>2</sub>O<sub>3</sub> NCs, and that the nucleation rate reaches a maximum at the early stage of the NC formation. In the low temperature regime (i.e., below ca. 230 °C), the nucleation rate of bcc-In<sub>2</sub>O<sub>3</sub> decreases gradually throughout the course of the synthesis, concurrently with the growth of the nucleated bcc-In<sub>2</sub>O<sub>3</sub> phase. At temperatures above ca. 230 °C, the rate of bcc-In<sub>2</sub>O<sub>3</sub> nucleation drops very rapidly after initial nuclei formation, and the mechanism of phase transformation is governed only by the growth of the new phase in the course of the reaction. The kinetics of phase transformation is correlated with the NC size (or the kinetics of NC growth), as evident from the size distribution histograms (Figure 1). It is very likely that defect sites at NC surfaces play a key role in the phase transformation process, owing to their lower activation energies.<sup>20</sup> The activation energy ( $E_a$ ) of the rh- to bcc-In<sub>2</sub>O<sub>3</sub> NC phase transformation can be determined from the calculated rate constant values for different temperatures, using the Arrhenius equation:

$$k = Ae^{-E_a/RT} \quad (3)$$

where  $A$  is the pre-exponential factor and  $R$  is the gas constant. The plot of  $\ln(k)$  versus  $1/T$  (Figure 3b) gives a value of  $153 \pm 20$  kJ/mol for the activation energy of the phase transformation of In<sub>2</sub>O<sub>3</sub> NCs.

Although the JMAEK model is applicable to many solid-state reactions, it is based on the assumption that samples have infinite sizes in addition to randomly distributed nucleation sites.<sup>26,27</sup> However, studies of phase transformation of TiO<sub>2</sub> polymorphs have revealed a strong dependence of the phase transformation rate on the grain size.<sup>32,33</sup> Furthermore, the nucleation mechanism responsible for the formation of a new phase may be dependent on temperature and/or the nature of the sample. Therefore, for detailed understanding of the phase transformation mechanism of nanocrystalline materials, which are finite in size, more precise models are needed. The choice of the suitable model often requires complementary structural information, particularly because different models can often be fitted to the same set of kinetic data.<sup>30,31</sup> High-resolution TEM (HRTEM) images of In<sub>2</sub>O<sub>3</sub> NCs at different reaction times during the synthesis at 230 °C are shown in Figure 4. Upon reaching 230 °C, the aliquots from the reaction mixture were removed and dispersed in toluene without any further treatment. The HRTEM image of the sample collected immediately upon reaching the reaction temperature (Figure

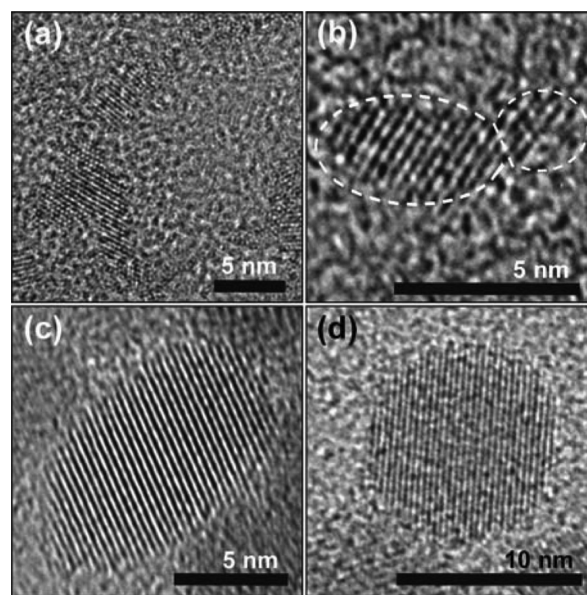


Figure 4. HRTEM images of In<sub>2</sub>O<sub>3</sub> NCs synthesized at 230 °C for (a) 0 min, (b) 10 min, (c) 1 h, and (d) 7 h. The boundaries of NCs in panel b are indicated with dashed line for clarity.

4a) shows that the sample has a network (polymer-like) morphology, which relatively quickly transforms into well-defined NCs with rh-In<sub>2</sub>O<sub>3</sub> crystal structure.<sup>19</sup> As the reaction continues, rh-In<sub>2</sub>O<sub>3</sub> NCs begin to interact, forming particle-particle interfaces (Figure 4b). At later stages of the reaction, the interacting NCs completely merge (Figure 4c) and eventually transform from elliptical to faceted quasi-spherical shape (Figure 4d). The process of NC interactions, observed by HRTEM, is accompanied by the transformation from rh-In<sub>2</sub>O<sub>3</sub> to bcc-In<sub>2</sub>O<sub>3</sub> phase, as demonstrated in Figure 1. Furthermore, the measured lattice spacing of NCs in Figure 4b–d ( $d \approx 2.92$  Å) corresponds to (222) plane of bcc-In<sub>2</sub>O<sub>3</sub> phase. Importantly, all NCs imaged by TEM exhibit only a single phase, without multiple domains or phase boundaries, indicating a very fast propagation of bcc-In<sub>2</sub>O<sub>3</sub> phase upon nucleation, which is consistent with recent theoretical investigations.<sup>40</sup> From these results and previous findings,<sup>19,38</sup> we can conclude that rh-In<sub>2</sub>O<sub>3</sub> NCs involving {110} lattice plane termination undergo phase transformation to bcc-In<sub>2</sub>O<sub>3</sub> terminated with {222} planes, which are the most stable set of planes of bcc-In<sub>2</sub>O<sub>3</sub>.<sup>41</sup> However, due to the random orientation of colloidal NCs and very fast phase propagation, determination of the crystallographic transformation pathways cannot be inferred from this work. Future theoretical and experimental studies are needed to address this topic.

To account for the role of surfaces and interfaces in nanocrystalline TiO<sub>2</sub> anatase to rutile phase transformation, the surface and interface nucleation kinetic models have been developed.<sup>28,29,33</sup> Which of the two mechanisms prevails depends largely on the concentration of particles.<sup>29</sup> For low-density particle packing, large free surface area is available, and the surface nucleation is a dominant mechanism. As the density of particle packing increases, the rate of interface nucleation at particle-particle contacts increases relative to the rate of the surface nucleation. Smaller particles which have a larger number of particle-particle contacts per unit volume exhibit higher interface nucleation rate. Furthermore, the phase nucleation mechanism is temperature dependent, and changes from

interface nucleation at low temperatures to surface nucleation at intermediate-to-high temperatures.<sup>29</sup> The rate of phase transformation for the interface nucleation model is therefore ultimately determined by the probability of the contact formation between two particles.<sup>29</sup> Investigation of the size dependence of phase transformation of TiO<sub>2</sub> polymorphs using the interface nucleation model shows that the activation energy changes very slightly with particle size, but the pre-exponential factor increases significantly with decreasing particle size.<sup>33</sup> The activation energy for interface nucleation is generally lower than that for surface nucleation. For example, for anatase TiO<sub>2</sub> particles having an average size of 7.9 nm,  $E_a$  values for interface and surface nucleation are 167 and 466 kJ/mol, respectively, in the temperature range 620–690 °C.<sup>29</sup>

On the basis of the TEM images showing NC contact formation (Figure 4) and the relatively low synthesis temperature in this work, we examined the kinetics of NC phase transformation in the framework of the interface nucleation model. The interface nucleation model for the kinetics of phase transformation can be expressed as:

$$\frac{(D_{rh}/D_0)^3}{(1-\alpha)} - 1 = (k_{IN}N_0)t \quad (4)$$

where  $D_{rh}$  is the average diameter of rh-In<sub>2</sub>O<sub>3</sub> NCs (Figure S5, Supporting Information),  $\alpha$  is the fraction of bcc-In<sub>2</sub>O<sub>3</sub> phase (vide supra), and  $k_{IN}$  is the kinetic constant for interface nucleation.  $N_0$  and  $D_0$  are the initial number and average diameter of rh-In<sub>2</sub>O<sub>3</sub> NCs, respectively. Figure 5a shows the

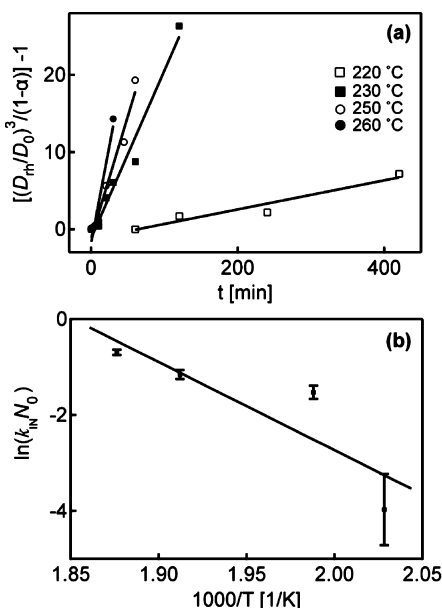


**Figure 5.** (a) Kinetic plots based on the interface nucleation model, generated from the fraction of the bcc-In<sub>2</sub>O<sub>3</sub> phase ( $\alpha$ ) present at different points in time in the samples synthesized at different temperatures. (b) Arrhenius plot based on the rate constants ( $k_{IN}$ ) obtained from the interface nucleation plot in (a).

linear fit of the interface nucleation model to the experimental data for the phase transformation of rh-In<sub>2</sub>O<sub>3</sub> to bcc-In<sub>2</sub>O<sub>3</sub> NCs. Largely linear dependence in Figure 5a confirms that phase transformation occurs predominantly by the interface nucleation mechanism in the temperature range investigated.<sup>29</sup> A significant contribution of the surface nucleation mechanism

would result in an exponential increase of the left-hand side of eq 4 with time.<sup>29</sup> The values of  $k_{IN}N_0$  obtained as fitting parameters for different temperatures are given in Table S2 (Supporting Information). The activation energy of the interface nucleation mechanism ( $E_{aIN}$ ) was determined to be  $152 \pm 60$  kJ/mol from the Arrhenius fitting to  $\ln(k_{IN}N_0)$  versus  $1/T$  dependence (Figure 5b). This value is in good agreement with the activation energy calculated using the JMAEK model, and is close to the values obtained for the anatase to rutile TiO<sub>2</sub> phase transformation by interface nucleation.<sup>29,42</sup>

Typically, the mechanism of a solid-state process is inferred by determining which model provides the best fit to the experimental kinetic data (model-fitting approach). Although each kinetic model is related to the specific type of process, it is often possible to apply more than one model to fit the experimental results. For isothermal solid-state processes different models can be fit to the same experimental data and used to calculate the activation energy,<sup>30,31</sup> allowing for deeper analysis of the role of different parameters in a given process. Consequently, the choice of the most suitable model should be supported by other complementary structural techniques. Electron microscopy imaging suggests that phase transformation of colloidal In<sub>2</sub>O<sub>3</sub> NCs occurs via the interface nucleation mechanism, by the formation of interfaces between metastable rh-In<sub>2</sub>O<sub>3</sub> NCs stabilized in an early stage of the reaction. According to the interface nucleation model, the transformation rate is determined by the nucleation of bcc-In<sub>2</sub>O<sub>3</sub> at the interface of two contacting rh-In<sub>2</sub>O<sub>3</sub> NCs. In conjunction with the JMAEK model analysis, we conclude that the nucleation of bcc-In<sub>2</sub>O<sub>3</sub> phase at the NC interface occurs rapidly at the beginning of the reaction, and that the nucleation rate decreases as the reaction progresses and the concentration of small rh-In<sub>2</sub>O<sub>3</sub> NCs diminishes. Higher reaction temperature enhances the probability of NC contact formation and bcc-In<sub>2</sub>O<sub>3</sub> phase nucleation, in addition to their growth, increasing the phase transformation rate (Figure 6a). At high reaction temperatures (above 250 °C), all nucleation events occur rapidly, and the phase transformation is completed within a short period of time, due to the rapid decrease in the number of small NCs. The NC size distribution results (Figure 1) support the conclusion that the fraction of small NCs in the reaction mixture decreases more dramatically at higher reaction temperatures. An increase in the concentration of rh-In<sub>2</sub>O<sub>3</sub> NCs also leads to an increase in the number of particle–particle contacts per unit volume, which speeds up the rate of the phase transformation (Figure 6b). The nucleation of the bcc-In<sub>2</sub>O<sub>3</sub> phase is most likely initiated by the interfacial defect sites. The similarity of the activation energy of phase transformation of TiO<sub>2</sub> nanocrystalline powder and colloidal In<sub>2</sub>O<sub>3</sub> NCs suggests that the nucleation of a thermodynamically stable phase in TCO NCs is determined by the interactions at a local or molecular level (which should be similar for different TCO NCs), rather than by macroscopic property of a material. Further increase in the reaction temperature would likely result in the gradual change of the phase transformation mechanism to the surface nucleation. The results of this analysis also indicate that phase transformation involving a decrease in the number of NCs in solution does not occur by the dissolution–recrystallization process.

To further study the effect of NC size on the phase transformation of In<sub>2</sub>O<sub>3</sub>, we performed in situ nonisothermal XRD analysis. For these measurements, the samples having different NC sizes were prepared, precipitated, and dried in the



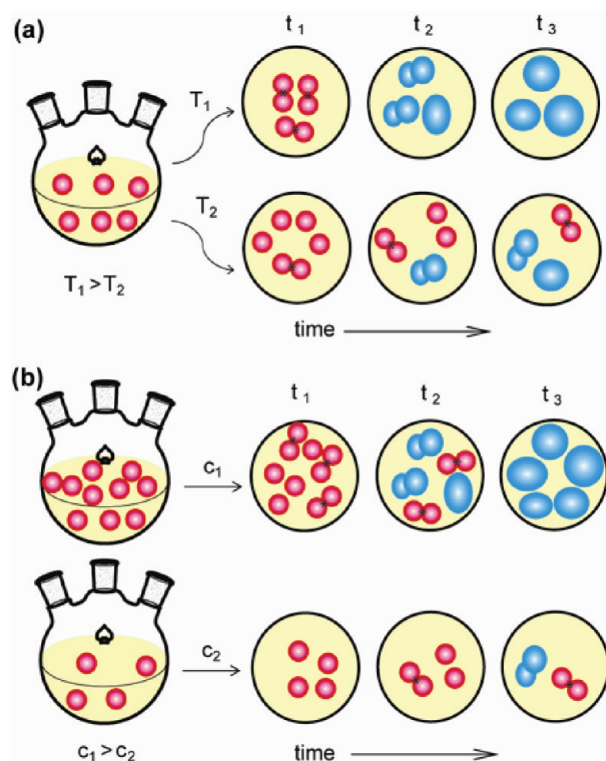


**Figure 6.** Schematic representation of the influence of (a) temperature ( $T$ ) and (b) NC concentration ( $c$ ) on the rate of phase transformation of  $\text{In}_2\text{O}_3$  NCs by the interface nucleation mechanism. Red and blue spheres indicate  $\text{rh-In}_2\text{O}_3$  and  $\text{bcc-In}_2\text{O}_3$  NCs, respectively, and asterisks (\*) indicate interface nucleation sites. The phase transformation rate is determined by the probability of contact formation between  $\text{rh-In}_2\text{O}_3$  NCs.

air. The resulting powder was heated in the X-ray diffractometer to different temperatures from 240 to 350 °C, and the XRD patterns were collected at each temperature. Figure 7a shows in situ XRD patterns of the sample prepared by the colloidal method at 150 °C for 30 h, as described in the Experimental Section. At the initial temperature of 240 °C, the NCs have corundum crystal structure and an average size of ca.

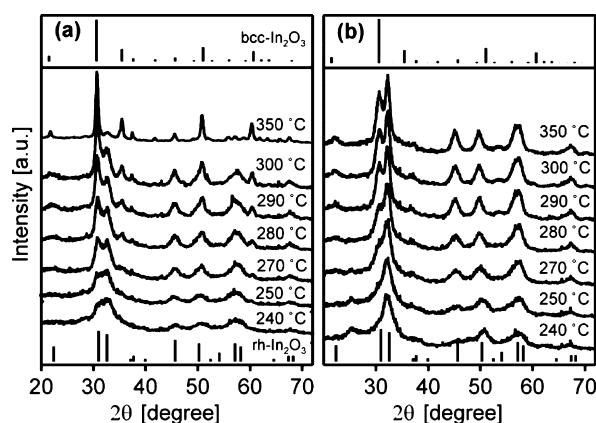


**Figure 7.** In situ variable-temperature XRD patterns of  $\text{In}_2\text{O}_3$  NCs synthesized by (a) colloidal method at 150 °C for 30 h, and (b) alcoholysis method in ethanol. Both samples were preheated at 240 °C in the diffractometer. The vertical lines are XRD peak positions of bulk  $\text{rh-In}_2\text{O}_3$  (bottom, JCPDS 21-0406) and  $\text{bcc-In}_2\text{O}_3$  (top, JCPDS 06-0416).

3 nm. Heating the sample at higher temperatures decreases the broadening of the XRD peaks, attesting to an increase in NC size, and induces a gradual phase transformation to  $\text{bcc-In}_2\text{O}_3$  NCs. At 350 °C, the cubic bixbyite phase becomes dominant. In situ phase transformation of larger  $\text{rh-In}_2\text{O}_3$  NCs, which were synthesized in ethanol by the alcoholysis method,<sup>35</sup> is shown in Figure 7b. These  $\text{rh-In}_2\text{O}_3$  NCs have an average size of ca. 5 nm at 240 °C, as calculated from the XRD peak broadening, although the sample contains some nanocrystalline  $\text{InOOH}$  intermediate.<sup>35</sup> Unlike smaller NCs in Figure 7a, this sample retains  $\text{rh-In}_2\text{O}_3$  structure throughout the studied temperature range (up to 350 °C), although NCs clearly increase in size during in situ heating. A comparison between the nonisothermal XRD results in Figure 7a and b suggests that the phase transformation rate is faster and requires less thermal energy for smaller NCs. This observation contrasts thermodynamic effects on the phase stabilization of NCs. Thermodynamically, a decrease in size of  $\text{In}_2\text{O}_3$  NCs leads to increased stabilization of  $\text{rh-In}_2\text{O}_3$  phase, owing to the surface energy and/or surface stress contributions.<sup>38</sup> The excess pressure caused by the surface stress increases with decreasing NC size, demanding more thermal energy to break and rearrange bonds in order to nucleate a new phase at NC surfaces.<sup>33</sup> An increase in the activation energy with decreasing NC size has been reported for the phase transformation of  $\text{TiO}_2$  and  $\text{In}_2\text{O}_3$  polymorphs.<sup>33,38</sup> The discrepancy between these thermodynamic predictions and the results of Figure 7 can be explained assuming that at low temperatures and for small initial NC sizes the dominant phase transformation mechanism is the interface nucleation, as discussed above. Smaller NCs have higher packing density relative to the larger ones, which increases the probability of particle–particle interactions and speeds up the phase transformation rate. Although metastable  $\text{rh-In}_2\text{O}_3$  phase is thermodynamically stabilized in NCs below ca. 5 nm in size, the phase transformation is kinetically controlled by the interface nucleation mechanism (i.e., probability of NC interaction), allowing smaller NCs to undergo phase transformation faster and at lower temperatures relative to larger NCs. Phase transformation under nonisothermal conditions was also studied in the solution phase by recording XRD patterns of the precipitated aliquots as the reaction mixture is heated at a rate of 1 °C/min (Figure S7, Supporting Information). Comparison with in situ XRD measurements of powder samples shown in Figure 7a reveals that the phase transformation of  $\text{In}_2\text{O}_3$  NCs in solution occurs at a lower temperature and a faster rate. This difference may be a consequence of increased probability of NC contact formation in solution, owing to their mobility. The synthesis and processing conditions may modify NC interactions and change the thermal energy of the phase transformation.

X-ray absorption spectroscopy can provide quantitative element-specific information about the local electronic structure environment, including surface sites,<sup>43</sup> and was used here to study the structure of  $\text{In}_2\text{O}_3$  NCs in the process of phase transformation. The local environment of  $\text{In}^{3+}$  sites during the phase transformation of  $\text{In}_2\text{O}_3$  NCs was systematically studied by In K-edge EXAFS method. Figure 8a shows Fourier-filtered EXAFS spectra of the sample synthesized at 250 °C, during the course of the reaction. These EXAFS spectra were derived for the In–O and In–In shells by the inverse Fourier transform of the pseudoradial functions (Figure S8, Supporting Information) in the range  $R = 1.15\text{--}3.37$  Å. The structural parameters obtained from the fitting of the EXAFS

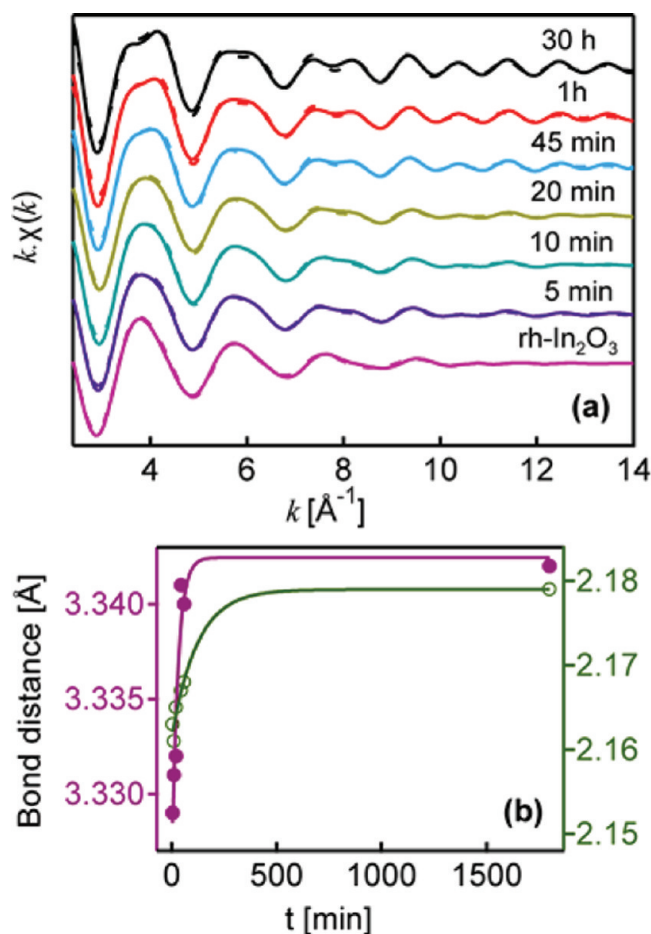


**Figure 8.** (a) Fourier-filtered In K-edge EXAFS spectra of  $\text{In}_2\text{O}_3$  NC samples synthesized at  $250^\circ\text{C}$  (solid lines), and the resulting curve fits (dashed lines) used to calculate structural parameters. The reaction times corresponding to each spectrum are shown in the graph. (b) In–O (green) and In–In (purple) bond distances calculated from the EXAFS analysis for NCs synthesized for different reaction times.

spectra are summarized in Table 2. For bulk  $\text{In}_2\text{O}_3$ , the cation–anion distances are nearly identical in both dimorphs, and a

**Table 2. Fitting Parameters Determined from the Analysis of EXAFS Spectra of  $\text{In}_2\text{O}_3$  NCs Synthesized at  $250^\circ\text{C}$**

$t$ (min)	In–O			In–In <sub>1</sub>			
	$N$	$R$ (Å)	$\sigma^2$ (Å <sup>2</sup> )	$N$	$R$ (Å)	$\sigma^2$ (Å <sup>2</sup> )	$\rho^b$ (%)
5	6.0	2.163	0.007	3.3	3.329	0.010	0.6
10	6.0	2.161	0.062	3.8	3.331	0.012	0.6
20	6.0	2.165	0.007	3.2	3.332	0.009	0.5
45	6.0	2.167	0.006	5.1	3.341	0.008	1.3
60	6.0	2.168	0.005	5.9	3.340	0.008	2.0
1800	6.0	2.179	0.006	6.0	3.342	0.005	2.5

<sup>a</sup>Debye–Waller factor. <sup>b</sup>Weighted residual factor.

small difference in density results from tighter packing of the anion layers in the corundum structure.<sup>44</sup> The average In–O bond length based on crystallographic data is 2.17–2.18 Å. In bulk rh- $\text{In}_2\text{O}_3$ , the In–In distance is 3.243 Å with the second shell coordination number (CN) of 3, while in bulk bcc- $\text{In}_2\text{O}_3$ , the In–In distance and CN are 3.35 Å and 6, respectively.<sup>44–46</sup> The average In–O and In–In bond distances for the samples isolated at different times during the synthesis are shown in

Figure 8b. Both In–O and In–In distances expand as the reaction proceeds. The increase in the average In–In distance can be attributed to the phase transformation from rh- $\text{In}_2\text{O}_3$  to bcc- $\text{In}_2\text{O}_3$ , based on the bulk values of this parameter. This conclusion is supported by the change in the second shell (In–In) CN from 3.3 to 6 (Table 2). However, In–O bond distance is much shorter in NCs at the beginning of the reaction than in bulk, and expands significantly in the relatively early stage of NC growth. Over the course of the reaction, the In–O bond distance reaches the value characteristic for the bulk  $\text{In}_2\text{O}_3$ . These results are consistent with an increase in surface stress with decreasing NC size, which is equivalent to an excess pressure, and compresses In–O bonds at NC surfaces. The increase in NC size with phase transformation reduces the surface stress and results in an expansion of In–O distances.

The ability to control crystal structure of polymorphic nanostructured materials is important for controlling their functional properties.<sup>47</sup> Photoluminescence in TCOs often arises from the structural defects, and is strongly dependent on the crystal structure.<sup>48</sup> Absorption and PL spectra of colloidal rh- $\text{In}_2\text{O}_3$  NCs synthesized for different durations at  $200^\circ\text{C}$  are shown in Figure 9. The PL bands are rather broad and exhibit

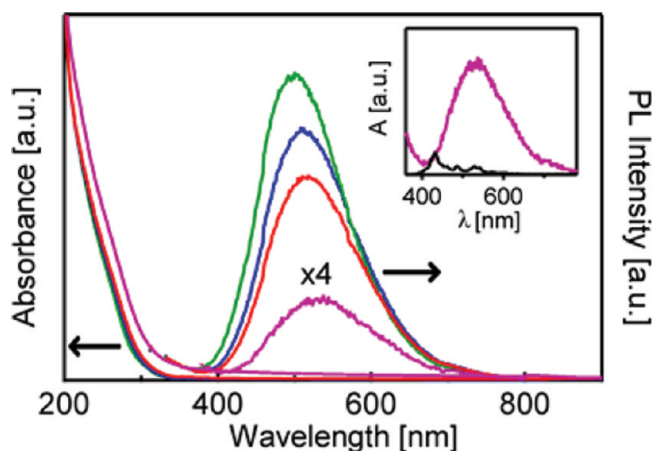


**Figure 9.** Absorption and PL spectra of colloidal rh- $\text{In}_2\text{O}_3$  NCs synthesized at  $200^\circ\text{C}$  for 1 (green), 4 (blue), 7 (red), and 30 h (purple). The spectra correspond to the same concentration of NCs. The spectrum of the sample synthesized for 30 h is shown multiplied by a factor of 4. Inset: PL spectra of colloidal rh- $\text{In}_2\text{O}_3$  NCs synthesized at  $200^\circ\text{C}$  for 30 h (purple) and bcc- $\text{In}_2\text{O}_3$  NCs synthesized at  $250^\circ\text{C}$  for 30 h (black).

large Stokes' shifts. With increasing synthesis time, the PL intensity decreases and the emission band shifts to lower energies. The PL intensity of the sample synthesized for 30 h is ca. 15 times smaller than the intensity of the sample synthesized for 1 h. The origin of  $\text{In}_2\text{O}_3$  emission has been attributed to the formation of the new energy levels in the band gap, due to oxygen vacancies.<sup>16,49,50</sup> Recent results suggest the donor–acceptor pair (DAP) recombination as a possible mechanism of PL in  $\text{In}_2\text{O}_3$ .<sup>37,51</sup> On the basis of the structural similarity with  $\text{Ga}_2\text{O}_3$ , the DAP mechanism in  $\text{In}_2\text{O}_3$  is assumed to involve oxygen vacancies and indium–oxygen vacancy pairs as donor and acceptor sites, respectively.<sup>48</sup> The decrease in the PL intensity accompanied by the red shift of the emission band can be attributed to an increase in the average donor–acceptor separation due to a decrease in the concentration of defects by NC annealing in solution.<sup>48</sup> Similarly to colloidal  $\text{Ga}_2\text{O}_3$  NCs,<sup>52</sup>



this emission is also sensitive to surface capping, which can influence the hole-trapping dynamics (Figure S9, Supporting Information). The PL properties of rh-In<sub>2</sub>O<sub>3</sub> NCs are significantly different from those of bcc-In<sub>2</sub>O<sub>3</sub> NCs, which show no such emission when synthesized by the described colloidal method (Figure 9, inset). This difference is likely associated with a lower concentration and/or different structure of defect sites in colloidal bcc-In<sub>2</sub>O<sub>3</sub> NCs. While detailed investigation of PL of In<sub>2</sub>O<sub>3</sub> NCs is beyond the scope of this work, our results suggest that the control of NC phase and defect formation during the synthesis plays a key role in tuning the emission properties.

## CONCLUSIONS

In summary, we studied the kinetics of phase transformation of rh-In<sub>2</sub>O<sub>3</sub> to bcc-In<sub>2</sub>O<sub>3</sub> NCs during colloidal synthesis. The kinetic data based on XRD and EXAFS measurements were investigated in the framework of JMAEK and interface nucleation models. The activation energy of phase transformation under isothermal conditions was found to be in excellent agreement for these two analyses ( $E_a \approx 152$  kJ/mol). Correlation of the kinetic results with TEM images of the product at different points in time during the reaction suggests that the phase transformation occurs by nucleation of bcc-In<sub>2</sub>O<sub>3</sub> at the interfaces between contacting rh-In<sub>2</sub>O<sub>3</sub> NCs. The nucleation rate reaches the maximum at an early stage of the reaction and consequently decreases due to a decrease in the concentration of small rh-In<sub>2</sub>O<sub>3</sub> NCs in the reaction mixture. The rate of phase transformation is critically dependent on both NC size and concentration; it increases with increasing concentration and decreasing size, owing to a higher probability of NC contact formation. Upon the nucleation of bcc-In<sub>2</sub>O<sub>3</sub>, which most likely occurs at the interfacial defect sites, the growth of the new phase propagates at a time scale which is much shorter than that examined in this study. This work demonstrates that phase transformation of In<sub>2</sub>O<sub>3</sub> NCs in solution is a kinetically controlled process, and provides improved understanding of the growth and phase transformation mechanism of oxide NCs. The results of this study allow for a rational manipulation of the NC surfaces and their interactions by controlling the reaction conditions, such as time and temperature, enabling the synthesis of colloidal NC building blocks with a desired crystal structure and properties.

## ASSOCIATED CONTENT

### Supporting Information

XRD patterns of bulk rh-In<sub>2</sub>O<sub>3</sub> and bcc-In<sub>2</sub>O<sub>3</sub>, TEM images of In<sub>2</sub>O<sub>3</sub> NCs synthesized at 230 and 260 °C, XRD patterns of mixed rh-In<sub>2</sub>O<sub>3</sub> and bcc-In<sub>2</sub>O<sub>3</sub> NC references, linear combination fitting of EXAFS spectra for In<sub>2</sub>O<sub>3</sub> NCs synthesized at 250 °C, plots of time dependence of In<sub>2</sub>O<sub>3</sub> NC size during syntheses, fits to the JMAEK equation, XRD patterns of In<sub>2</sub>O<sub>3</sub> NCs synthesized under nonisothermal conditions, Fourier transform EXAFS spectra of In<sub>2</sub>O<sub>3</sub> NCs synthesized at 250 °C, PL spectra of In<sub>2</sub>O<sub>3</sub> NCs synthesized for 30 h before and after the TOPO treatment (Figures S1–S9). Values of  $k_{IN}N_0$  determined from the interface nucleation model plot, and average NC sizes obtained from TEM images for rh-In<sub>2</sub>O<sub>3</sub> and bcc-In<sub>2</sub>O<sub>3</sub> NCs (Tables S1 and S2). This material is available free of charge via the Internet at <http://pubs.acs.org>.

## AUTHOR INFORMATION

### Corresponding Author

pavler@uwaterloo.ca

### Notes

The authors declare no competing financial interest.

## ACKNOWLEDGMENTS

This work was supported by the Natural Sciences and Engineering Research Council of Canada (NSERC) Discovery Grant, Canada Foundation for Innovation and Ontario Research Fund. P.V.R. thanks Canada Research Chairs Program (NSERC) and Ontario Ministry of Economic Development and Innovation (Early Researcher Award) for partial support of this work. S.S.F. acknowledges Waterloo Institute for Nanotechnology for the Graduate Research Fellowship and the Canadian Light Source for the Graduate Travel Award. TEM measurements were performed at the Canadian Centre for Electron Microscopy in the Brockhouse Institute for Materials Research at McMaster University. X-ray absorption spectroscopy measurements described in this paper were performed at the Canadian Light Source, which is supported by NSERC, NRC, CIHR, and the University of Saskatchewan. We thank Drs. Ning Chen and Weifeng Chen for their assistance with XAS measurements and Prof. Eric Prouzet (University of Waterloo) for helpful discussions.

## REFERENCES

- (1) McHale, J. M.; Auroux, A.; Perrotta, A. J.; Navrotsky, A. *Science* **1997**, *277*, 788–791.
- (2) Chen, C.-C.; Herhold, A. B.; Johnson, C. S.; Alivisatos, A. P. *Science* **1997**, *276*, 398–401.
- (3) Navrotsky, A.; Mazeina, L.; Majzlan, J. *Science* **2008**, *319*, 1635–1638.
- (4) Tolbert, S. H.; Alivisatos, A. P. *Annu. Rev. Phys. Chem.* **1995**, *46*, 595–625.
- (5) Zhang, H.; Banfield, J. F. *J. Mater. Chem.* **1998**, *8*, 2073–2076.
- (6) Chraska, T.; King, A. H.; Berndt, C. C. *Mater. Sci. Eng., A* **2000**, *286*, 169–178.
- (7) Wan, Q.; Dattoli, E. N.; Fung, W. Y.; Guo, W.; Chen, Y.; Pan, X.; Lu, W. *Nano Lett.* **2006**, *6*, 2909–2915.
- (8) Baxter, J. B.; Aydil, E. S. *Appl. Phys. Lett.* **2005**, *86*, 053114.
- (9) Noguchi, S.; Sakata, H. *J. Phys. D: Appl. Phys.* **1980**, *13*, 1129–1133.
- (10) Elam, J. W.; Baker, D. A.; Martinson, A. B. F.; Pellin, M. J.; Hupp, J. T. *J. Phys. Chem. C* **2008**, *112*, 1938–1945.
- (11) Shannon, R. D. *Solid State Commun.* **1966**, *4*, 629–630.
- (12) Karazhanov, S. Z.; Ravindran, P.; Vajeeston, P.; Ulyashin, A.; Finstad, T. G.; Fjellvåg, H. *Phys. Rev. B* **2007**, *76*, 075129.
- (13) Gurlo, A.; Kroll, P.; Riedel, R. *Chem.—Eur. J.* **2008**, *14*, 3306–3310.
- (14) Epifani, M.; Siciliano, P.; Gurlo, A.; Barsan, N.; Weimar, U. *J. Am. Chem. Soc.* **2004**, *126*, 4078–4079.
- (15) Ashok, V. D.; De, S. K. *J. Phys. Chem. C* **2011**, *115*, 9382–9392.
- (16) Yu, D.; Yu, S.-H.; Zhang, S.; Zuo, J.; Wang, D.; Qian, Y. *Adv. Funct. Mater.* **2003**, *13*, 497–501.
- (17) Chen, C.; Chen, D.; Jiao, X.; Wang, C. *Chem. Commun.* **2006**, 4632–4634.
- (18) Lee, C. H.; Kim, M.; Kim, T.; Kim, A.; Paek, J.; Lee, J. W.; Choi, S. Y.; Kim, K.; Park, J.-B.; Lee, K. *J. Am. Chem. Soc.* **2006**, *128*, 9326–9327.
- (19) Farvid, S. S.; Dave, N.; Radovanovic, P. V. *Chem. Mater.* **2010**, *22*, 9–11.
- (20) Khawam, A.; Flanagan, D. R. *J. Phys. Chem. B* **2006**, *110*, 17315–17328.
- (21) Hulbert, S. F. *J. Br. Ceram. Soc.* **1969**, *6*, 11–20.

- (22) Christian, J. W. *The Theory of Transformations in Metals and Alloys: An Advanced Textbook in Physical Metallurgy*; Pergamon Press: Oxford, 1965; Vol. 7.
- (23) Avrami, M. *J. Chem. Phys.* **1939**, *7*, 1103–1112.
- (24) Choi, S. Y.; Mamak, M.; Speakman, S.; Chopra, N.; Ozin, G. A. *Small* **2005**, *1*, 226–232.
- (25) Kirsch, B. L.; Richman, E. K.; Riley, A. E.; Tolbert, S. H. *J. Phys. Chem. B* **2004**, *108*, 12698–12706.
- (26) Avrami, M. *J. Chem. Phys.* **1940**, *8*, 212–224.
- (27) Weinberg, M. C.; Birnie, D. P.; Shneidman, A. V. *J. Non-Cryst. Solids* **1997**, *219*, 89–99.
- (28) Zhang, H.; Banfield, J. F. *Am. Mineral.* **1999**, *84*, 528–535.
- (29) Zhang, H.; Banfield, J. F. *J. Mater. Res.* **2000**, *15*, 437–448.
- (30) Zhou, D.; Grant, D. J. W. *J. Phys. Chem. A* **2004**, *108*, 4239–4246.
- (31) Khawam, A.; Flanagan, D. R. *J. Pharm. Sci.* **2006**, *95*, 472–498.
- (32) Gribb, A. A.; Banfield, J. F. *Am. Mineral.* **1997**, *82*, 717–728.
- (33) Zhang, H.; Banfield, J. F. *Chem. Mater.* **2005**, *17*, 3421–3425.
- (34) Zhang, H.; Banfield, J. F. *J. Phys. Chem. B* **2000**, *104*, 3481–3487.
- (35) Chu, D.; Zeng, Y.-P.; Jiang, D.; Xu, J. *Nanotechnology* **2007**, *18*, 435605.
- (36) Michalowicz, A.; Moscovici, J.; Muller-Bouvet, D.; Provost, K. *J. Phys.: Conf. Ser.* **2009**, *190*, 012034.
- (37) Farvid, S. S.; Wang, T.; Radovanovic, P. V. *J. Am. Chem. Soc.* **2011**, *133*, 6711–6719.
- (38) Farvid, S. S.; Dave, N.; Wang, T.; Radovanovic, P. V. *J. Phys. Chem. C* **2009**, *113*, 15928–15933.
- (39) Gurlo, A. *Angew. Chem., Int. Ed.* **2010**, *49*, 5610–5612.
- (40) Grunwald, M.; Dellago, C. *Nano Lett.* **2009**, *9*, 2099–2102.
- (41) Walsh, A.; Catlow, C. R. A. *J. Mater. Chem.* **2010**, *20*, 10438–10444.
- (42) Kumar, K.-N. P.; Keizer, K.; Burggraaf, A. J. *J. Mater. Chem.* **1993**, *3*, 1141–1149.
- (43) Chen, L. X.; Rajh, T.; Jager, W.; Nedeljkovic, J.; Thurnauer, M. C. *J. Synchrotron Radiat.* **1999**, *6*, 445–447.
- (44) Prewitt, C. T.; Shannon, R. D.; Rogers, D. B.; Sleight, A. W. *Inorg. Chem.* **1969**, *8*, 1985–1993.
- (45) Nadaud, N.; Lequeux, N.; Nanot, M.; Jove, J.; Roisnel, T. *J. Solid State Chem.* **1998**, *135*, 140–148.
- (46) Parent, P.; Dexpert, H.; Tourillon, G.; Grimal, J.-M. *J. Electrochem. Soc.* **1992**, *139*, 276–281.
- (47) Wang, T.; Radovanovic, P. V. *J. Phys. Chem. C* **2011**, *115*, 406–413.
- (48) Wang, T.; Farvid, S. S.; Abulikemu, M.; Radovanovic, P. V. *J. Am. Chem. Soc.* **2010**, *132*, 9250–9252.
- (49) Liu, Q.; Lu, W.; Ma, A.; Tang, J.; Lin, J.; Fang, J. *J. Am. Chem. Soc.* **2005**, *127*, 5276–5277.
- (50) Liang, C.; Meng, G.; Lei, Y.; Phillipp, F.; Zhang, L. *Adv. Mater.* **2001**, *13*, 1330–1333.
- (51) Guha, P.; Kar, S.; Chaudhuri, S. *Appl. Phys. Lett.* **2004**, *85*, 3851–3853.
- (52) Wang, T.; Radovanovic, P. V. *J. Phys. Chem. C* **2011**, *115*, 18473–18478.